electronics

MDPI

Article

SDR-Enabled Multichannel Real-Time Measurement System for In Situ EMF Exposure Evaluation

Annamaria Sârbu [1,*], Marco Donald Migliore [2], Emil Șorecău [1,3], Mirela Șorecău [1,3], Simona Miclăuș [1] and Paul Bechet [1]

[1] Communications, IT and Cyber Defense Department, "Nicolae Bălcescu" Land Forces Academy, 550170 Sibiu, Romania
[2] Department of Electrical and Information Engineering, University of Cassino and Southern Lazio, 03043 Cassino, Italy
[3] Department of Electrotechnics and Measurements, Technical University of Cluj Napoca, 400114 Cluj-Napoca, Romania
* Correspondence: paljanosanna@yahoo.com

Abstract: The spatial and temporal variability of the signals emitted by modern communication devices produced a paradigm shift in approaching the human exposure to electromagnetic fields (EMF). This inherent variability requires in situ, agile EMF measurement solutions capable of performing real-time isotropic measurements. The aim of this paper is to describe a new real-time, highly flexible multichannel EMF measurement system that consists of a sensor connected to state-of-the-art software-defined radio (SDR) equipment. In this paper an electric field sensor is proposed, but we also provide information on the extension of the probe to electric and magnetic fields. In the receiver section, the proposed solution is compared in terms of performances (sensitivity and accuracy), costs, and requirements, with standard solutions based on spectrum analyzers or a digital oscilloscope. Finally, the proposed solution was tested considering the signals emitted in various operating scenarios by a mobile device operating in the LTE-A and IEEE 802.11ax mobile communication standards. The results confirm the versatility and efficiency of the proposed solution for in situ EMF measurements of signals emitted by the new generation communication devices.

Keywords: in situ exposure evaluation; multichannel EMF measurements; software defined radio; spectrum analyzer; digital oscilloscope

Citation: Sârbu, A.; Migliore, M.D.; Șorecău, E.; Șorecău, M.; Miclăuș, S.; Bechet, P. SDR-Enabled Multichannel Real-Time Measurement System for In Situ EMF Exposure Evaluation. *Electronics* **2022**, *11*, 2670. https://doi.org/10.3390/electronics11172670

Received: 29 July 2022
Accepted: 23 August 2022
Published: 26 August 2022

1. Introduction

Today's 5th Generation New Radio (5G NR) introduces significant enhancements in characteristics such as flexibility, scalability, and efficiency, both in terms of power usage and spectrum. The end user experiences are boosted by employing new frequency resources and spectrum-sharing techniques combined with strong cell densification. The system 5G NR uses an optimized access scheme based on cyclic prefix orthogonal frequency division multiplexing (CP-OFDM) together with beamforming and Multi-User Multiple Input Multiple Output (MU-MIMO). As they are being implemented, 5G NR systems are designed to operate within several bands comprising frequencies below 6 GHz (most of the rolled out commercial networks in Europe) up to 66–71 GHz [1].

The densification of the mobile network architecture due to the newly implemented 5G NR communication technologies is continuously raising concerns on the possible health effects of EMFs. The technological advent that we are facing nowadays urges for a relevant characterization of user exposure to such complex EMFs. As an example, relevant methodologies for assessing 5G base station exposure were developed in [2,3].

The standards concerning human exposure to EMFs were recently updated to cover for the emerging applications [4,5]. According to the standards, specific absorption rate (SAR) measurements must be conducted for compliance with the guidelines' basic restrictions.

The SAR is a measure of the rate of EMF energy deposition inside tissues, and restrictions based on this metric consider solely the thermal effect of the EMF. As SAR measurements are impossible to conduct in vivo, the regulatory standards also provide external limits in terms of reference levels that are more-easily assessable. Above 2 GHz, the reference level for the averaged local exposure to EMFs (duration longer than 6 min) is expressed in terms of incident power density (PD) expressed in W/m^2. Additionally, for averaging time intervals shorter than 6 min, ICNIRP introduced the incident energy density (in J/m^2) as a reference level for local exposure [4]. To determine the incident energy density, one must access the temporal variation of signal power in time, a requirement which becomes complicated as the frequency bandwidth enabled by the modern communications standards continuously expands.

Different types of measurement systems are currently available on the market that can experimentally determine either the SAR, the incident electric (E) field strength, or the PD [6]. These include E-field probe-based systems [7], electro-optical probe-based systems [8], and optical fiber thermal sensor-based systems [9]. In addition, a series of non-invasive measurement systems such as infrared measurement systems [10], thermal scanner systems [11], PD measurements [12], and optical SAR systems [13] also exist. According to a recent sounding review in the field of radiofrequency (RF) exposure assessment, the major uncertainties in the exposure assessment are likely to be related to the inherent variability of real-world exposures, rather than imprecision in measurement techniques [14]. Moreover, with the increasing number of mobile subscribers, there are studies that indicate that the user exposure is dominated by the own or neighboring mobile equipment [15,16]. With 5G NR, the importance of self-produced exposure increases both due to uplink (UL) and downlink (DL) signals contributions [17]. Therefore, this requires extensive in situ EMF measurements to be performed in the proximity of user equipment.

Several methods are available for assessing the incident PD in the proximity of a device [18]. The first proposed method requires the measurement of both E and magnetic (H) fields on an evaluation surface. To this extent, E and H fields are measured sequentially and then combined to calculate the local PD value. This activity is extremely time consuming since both field strengths must be measured in all three orthogonal directions, and their time-variability counted continuously. To overcome this issue, a phase reconstruction algorithm was proposed in [19]. The method refers to the measurement of the E-field component (both amplitude and phase) at a larger distance from the evaluation surface followed by the field back-projection. These systems can be used in laboratory conditions with controlled experimental setups to characterize antennas or perform compliance assessments. However, the mentioned methods are not applicable for in situ measurements, in the proximity of mobile devices, that require the simultaneous retrieval of the orthogonal vector-field components.

Most commercially available field probes that can be used for frequency selective measurements are unidirectional [7], but some electronically switched isotropic probes/antennas are also available [20,21]. The size of the probes (415 mm × 87 mm—by R&S) does not recommend them for proximity measurements because of the low spatial resolution and significant field alteration. To measure the total field strength arising from all directions, typical isotropic sensors consist of three orthogonally aligned probes that are electronically switched on [22]. However, besides the probe's dimension, the dwell time or switching time of current isotropic antennas (10 μs) [20] appears to be inadequate for the fast symbol variation of 5G NR technology—where the symbol duration is 16.67 μs for a 60 kHz subcarrier spacing [23].

To solve the issue of the simultaneous retrieval of E-field vector components, we proposed a sensor prototype based on orthogonally positioned miniature near-field probes. The close positioning of the probes makes them susceptible to mutual coupling even in the receiving mode [24]. Thus, we can analytically analyze the mutual coupling phenomenon and evaluate the mutual coupling errors based on an original approach that requires the measurement of the probes scattering parameters (S).

The proposed sensor must be connected to suitable frequency selective equipment to enable a real-time multichannel EMF field measurement with an adequate time response corresponding to the minimum time variations of the investigated communication technologies. Traditionally, for frequency-selective in situ measurements, spectrum analyzers (SA) are employed [25,26]. With recent technological development, multi-channel instruments such as oscilloscopes [27] and software-defined radio (SDR) transceivers [28,29] became a viable alternative for EMF measurements. Therefore, in this paper, we propose an SDR-enabled real-time multichannel measurement system to be used for in situ EMF exposure evaluations. The measurement system is analyzed, characterized, and compared to the standard solution of using SAs and a multichannel digital oscilloscope (DO). After calibration and validation, the SDR-enabled measurement system was used for an in situ measurement campaign of a mobile device operating in the LTE-A and IEEE 802.11ax communication standards under different operating scenarios.

The motivation of this research originates from the need to obtain synchronous real-time isotropic responses from the orthogonal field dipoles. This is required to eliminate the switching time spans between the sensor elements and to obtain a true real-time isotropic capability. Moreover, the designed measurement system must be flexible, agile, and customized for in situ measurement campaigns. Therefore, the novelty of our approach consists of a multichannel measurement system capable of retrieving simultaneous E- and/or H-field components. This advances the current isotropic measurement systems which are based on switching between the probes by providing the real-time simultaneous determination of highly stochastic signals on all three spatial axes followed by the further computation of the total E-field strength. In addition, we comparatively analyzed the measurement systems' performance, cost, and suitability with respect to the accurate evaluation of 5G/6G-emitted fields in the proximity of mobile devices.

The remainder of the paper is structured as follows: the materials and methods section, which is divided in two subsections dedicated to the sensor and measurement instrumentation, the results and discussion section divided into three subsections, and the conclusions.

2. Materials and Methods

2.1. The Proposed Sensor

In this section a compact three-axial probe able to measure the three components of the E field will be discussed in detail.

Since the complete analysis of the E/H field requires a 6-channel measurement system, not available during the measurement sessions, in this work, we will focus our attention on the E-field probe solution. However, it should be noted that the geometry lends itself to the realization of a sensor for measuring both the E and H field, as will be briefly discussed in this section.

The E-field sensor is composed of three identical orthogonally positioned probes, offering an isotropic response in 1–6 GHz frequency band with low perturbation of the incident field. It was built using 3 identical miniature commercial field probes (PBS-1 set from Aaronia A.G.) [30].

The position of the probes was chosen to maintain orthogonal positions between the 3 cartesian axes by fixing the probes on a custom-made plexiglass tripod. Since their tips could not be superimposed practically, a very small air volume gap was delimited by the dimensions of the tips during the measurements. Based on the probe tip dimensions and the distance between the probes, the measurement volume was defined as a sphere with a radius of 1 cm. Figure 1a presents a schematic description of the designed E-field sensor and its intended connections.

As noted above, the geometry of the sensor also represents a good starting point for a three-axial E- and H-field probe, that is currently under development. This can be obtained by adding three orthogonal coil antennas, as shown in Figure 1b.

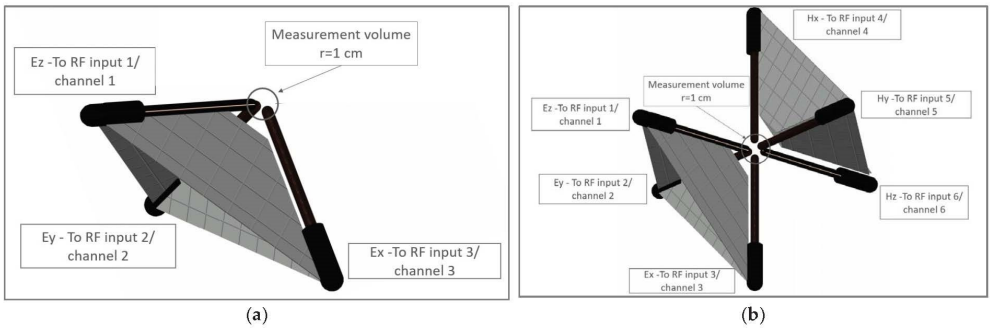

Figure 1. Schematic description of the proposed E-field sensor (**a**) and E- and H-field sensor (**b**).

The close positioning of the probe dipoles can cause mutual coupling, which could limit the effectiveness of the probe [31]. Mutual coupling is usually analyzed in transmission mode, while analysis in reception mode is less commonly discussed. An accurate evaluation can be obtained using full-wave simulations. Numerical simulations are a powerful tool that, however, suffer from some drawbacks. The solution depends on the specific incident field that changes with the imping direction in case of simple single plane wave, and in more complex way in case of there not being plane-wave incident field. Furthermore, the numerical solution makes it difficult to clarify the mechanisms at the basis of the mutual coupling, whose understanding can be useful in the design of the probe.

In the following, we will follow a different approach, that is, new at the best knowledge of the authors, based on a simplified analysis of the problem. Even if the solution suffers from some approximations, this approach has the advantage to give some insights of the physics of the problem and to give a simple estimation of the impact of the mutual coupling on the measured quantity.

With reference to a harmonic regime, let us consider an antenna in reception mode, (Figure 2) closed on a load having impedance Z_L that models the receiver. The antenna can be modeled as a Thevenin circuit [31], wherein V_0 is voltage at the gap of the antenna closed on an open circuit, and Z_{IN} is the input impedance of the antenna in reception mode. The energy dissipated on the load Z_L is the 'useful' energy, i.e., the energy available for applications. However, Z_{IN} also has a real part, and consequently, some energy dissipates on the impedance Z_{IN}. This energy is re-irradiated by the antenna. In general, the re-irradiated energy depends on the mismatch between the two impedances Z_L and Z_{IN}. In case of perfectly matched load ($Z_L = Z_{IN}^*$), the re-irradiated energy is equal to the energy absorbed by the load.

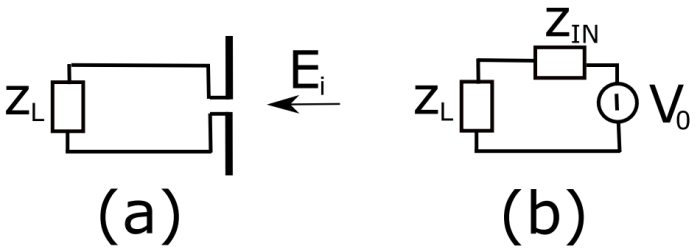

Figure 2. Circuit with antenna in receive mode; (**a**) schematic diagram; (**b**) circuit diagram Even if the re-irradiated energy is quite small, it can be received by antennas that are very close to the re-irradiating antenna, causing mutual coupling. The analysis of mutual coupling for receiving antennas is quite complex. In the following, we will introduce a simplified model that allows us to have a rough idea of the impact of the mutual coupling.

With reference to Figure 3, let us consider a simple model consisting of two receiving elements placed at very close distance, and an incident plane wave E_i (blue arrow). Note that the incident field on the two antennas (antenna 1 and antenna 2) have same amplitude, but different phases, depending on the direction of the plane wave. The field on the

two antennas will be called E_{i1} and E_{i2}, wherein $E_{i1} = E_{i2}\ exp(j\varphi)$, φ being the phase difference. Two different coordinate systems (z_1 and z_2) are used for the two antennas to have voltage definitions coherent with the standard definitions using in-microwave scattering parameters S, which will be used in the following discussion.

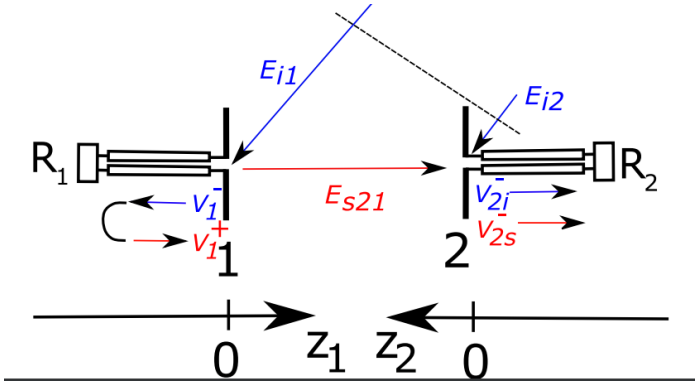

Figure 3. Scheme of mutual coupling in receive mode (2 antennas).

Let us consider antenna 1. The incident field E_{i1} excites a voltage wave $V_1{}^- = k_1\ E_{i1}$ (k_1 being a quantity representing the response in amplitude and phase of the antenna 1, this quantity depends on the direction of propagation and polarization of the incident field) traveling from the antenna toward the load (i.e., the receiver R_1). In field level measurement systems, antennas are matched to the receiver. Accordingly, in the following, we suppose that half the energy is absorbed by the load, while the other half is re-radiated by the antenna. Accordingly, we suppose a voltage wave $V_1{}^+$, having amplitude equal to $|V_1{}^-|/\sqrt{2}$ amplitude, which feeds antenna 1, causing a field E_{S21} incident on antenna 2.

In practice, antenna 2 received two contributions, E_{i2} and E_{S21}. The voltage on the receiver (i.e., R_2) is the interference between the two voltage waves $V_{2i}{}^-$ and $V_{2s}{}^-$ associated to E_{i2} and $E_{S21}{}^-$.

The antenna 1 and antenna 2 system can be modeled as a two-port linear microwave device, whose input–output relationships can be modeled using S scattering coefficients [32]. The scattering coefficient S_{21} is defined as $S_{21} = V_2{}^-/V_1{}^+$ when no voltage waves travel from the receiver R2 toward antenna 2. Accordingly, we have that the scattered field E_s gives a voltage wave at the gap of antenna 2 equal to $V_{2s}{}^+ = V_1{}^+\ S_{21} = k_2\ E_{i1}\ S_{21}/\sqrt{2}$, while the incident field E_i on antenna 2 gives a wave voltage equal to $V_{2i}{}^+ = k_2\ E_{i2}$. Note that k_2 is generally different from k_1 since they generally depend on the orientation of the antennas in the space with respect to the incident field. The voltage at the gap of the antenna is $V_2{}^+ = (k_2\ E_{i2} + k_1\ E_{i1}\ S_{21}/\sqrt{2})$. To have a rough estimation, let us suppose that $k_1 \approx k_2 = k$. In this case, we have $V_2{}^+ \approx k\ E_{i2}\ (1 + S_{21}\ exp(j\varphi)/\sqrt{2})$ instead of $k\ E_{i2}$, that is, the value in absence of mutual coupling. Since the phase of the second term is not known, the relative measured quantity ranges in

$$\Delta E \approx \left(k\left|E_{i2}\right|\left(1 \pm S_{21}/\sqrt{2}\right)\right)/(k|E_{i2}|) = 1 \pm S_{21}/\sqrt{2} \quad (1)$$

It must be noted that this is a highly simplified model. For example, the presence of antenna 2 also modifies the currents on antenna 1, mismatches between the antenna and the load change the re-irradiated energy, short antennas used in field measurements usually have losses (that help to enlarge the bandwidth avoiding too much deep resonances), and so on. Despite the simplifications, the model can give a rough but useful indication of the uncertainty affecting the measurements due to the mutual coupling.

Coming back to the E-field probe proposed in this paper, it is modeled as a 3-ports (the three antennas) microwave network, where each port represents the antenna terminal. The resulting S parameter matrix is presented in (2).

$$S = \begin{bmatrix} S_{11}S_{12}S_{13} \\ S_{21}S_{22}S_{23} \\ S_{31}S_{32}S_{33} \end{bmatrix} \quad (2)$$

where in S_{ij} is the parameter that corresponds to the wave voltage traveling from port j to port i when all the other ports are closed on perfectly matched loads. Low S_{ij} values are an indication of a low coupling among the antennas. Loosely speaking, it is of interest to obtain also low S_{ii} values, with S_{ii} being the i-th reflection coefficient of the i-th antenna with all the other antennas closed on a matched load.

The scattering parameters can be measured using Vector Network analyzers (VNA). We used a 2-port VNA, model R&S ZNB 40, by alternatively connecting all sensor probes to the two VNA ports. During the measurements, the ports that were not connected to the VNA, were connected to a 50 Ω impedance. The VNA was calibrated in the frequency range 0.8–6 GHz, with 100,000 measurement points being taken for each sweep. The frequency resolution in the interest bandwidth was 50 kHz. The VNA power was set to −20 dBm, which is the highest signal level usually measured around our interest RF sources by these probes. Figure 4a presents the setup used during the S parameters measurement.

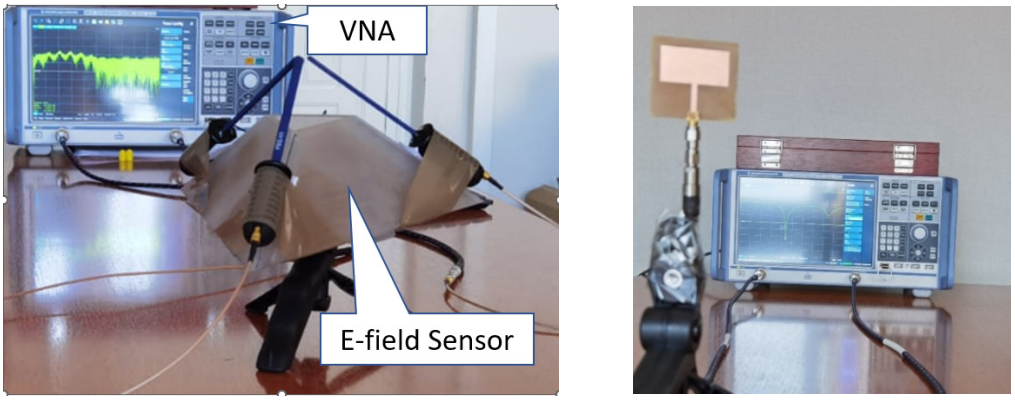

(**a**) (**b**)

Figure 4. (**a**) S parameters measurement setup; (**b**) S11 measurement setup for the patch antenna.

Finally, to evaluate the influence of the sensor on emitting equipment we have investigated the variation of the reflection S11 parameter for a custom-made patch antenna in the presence of the sensor placed at 1, 2 and 3 cm distance, respectively, in the absence of the sensor. The patch antenna was first designed using CST Studio Suite Software and then printed on a printed circuit board (PCB). Figure 4b presents the S11 measurement setup of the patch antenna using the R&S VNA.

2.2. Receiver Section

To simultaneously measure the three E-field components, a novel measurement solution based on a multichannel SDR having at least 3 synchronized radiofrequency channels was developed. In particular, the USRP (Universal Software Radio Peripheral) N310, state-of-the-art SDR multichannel equipment, was selected to complete the measurement system which is presented in Figure 5a.

The field in the setup presented in Figure 5a was generated by a signal generator model R&S SMBV 100 A equipped with option SMBV-K85 for Long Term Evolution-Advanced (LTE-A) signal generation connected to an Aaronia HyperLog 4060 directive antenna. This solution allowed to simulate an LTE-A uplink signal having a channel bandwidth of 20 MHz (100 Resource Blocks (RB)/slot) with Quadrature Phase Shift Keying (QPSK) modulation format.

(**a**) (**b**)

Figure 5. (**a**) SDR-enabled measurement system, (**b**) SA-enabled measurement system.

Three RF channels of the USRP were connected to the corresponding elements of the E-field probes. The USRP was connected via a 10 Gb Ethernet connection to the PC running an Ubuntu operating system. A GNU Radio flowchart was constructed to perform channel power (CP) measurements—Figure 6.

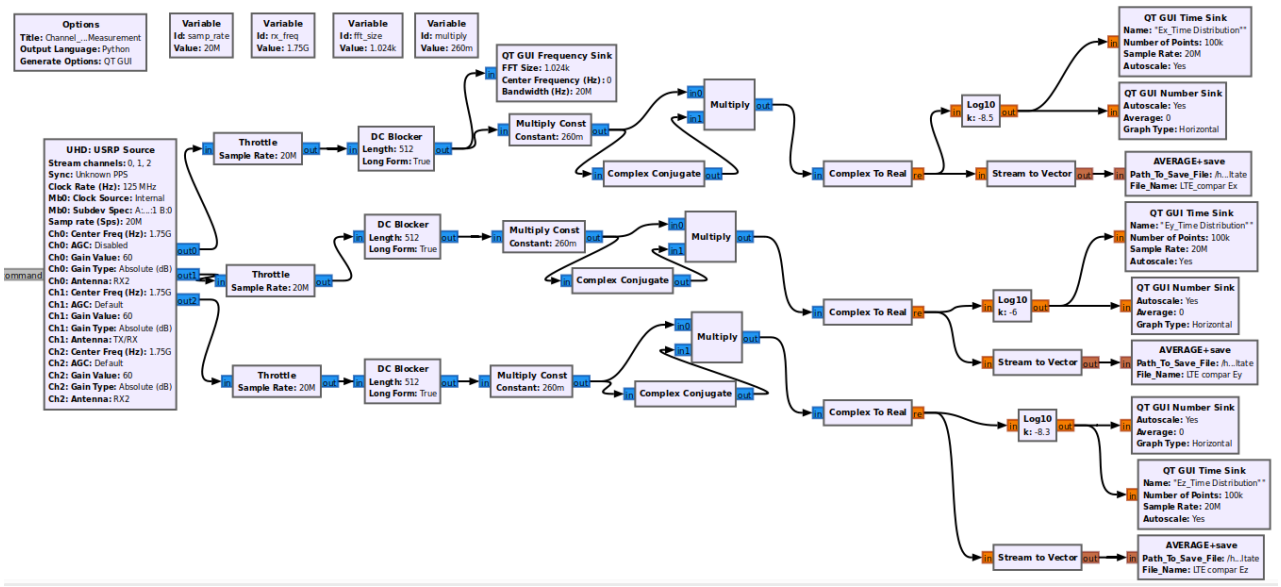

Figure 6. GNU Radio flowchart used for CP measurements using the SDR (USRP N310).

GNU Radio is a free software development framework that provides signal processing functions for SDR. It is used by hobbyist and academia and supports both wireless communications research and operational radio systems. The latest applications of GNU Radio environment include near-field measurements [33], wireless communication system development [34,35], spectrum sensing and availability [36,37], and machine learning [37,38].

The CP was measured based on the SDR capability to access the signal samples in the time domain. The instantaneous power level of the signal was calculated as the square root of the product between the sample power represented in complex form and its conjugate [39]. We have designed a user interface that enables both time and frequency visualization of the measured signal samples, as well as the calculated CP value. The instantaneous power values are inputted to a custom programmed block for data averaging and saving. The limitations of this USRP model in reporting accurate field levels and calibration procedures were analyzed in [28].

The SDR-enabled measurement system was tested by performing measurements on signals emitted by a mobile phone model Huawei P40 Pro (DUT). The DUT was sequentially

measured while operating in Long Term Evolution-Advanced (LTE-A) communication standard and in the IEEE 802.11ax Wi-Fi standard.

During the LTE connectivity, the DUT was connected to the public designated base station and three experimental scenarios were considered:

- file upload (large video files sent over WhatsApp)
- streaming (YouTube 4k video at 720 p)
- speed test (using a free available speed test app [40]).

For the Wi-Fi connectivity, the DUT was connected to an IEEE 802.11ax Wi-Fi router model TP-Link Archer AX10 operating in the 5 GHz frequency range (placed in the same room at 5 m distance from the DUT). During the Wi-Fi connectivity four experimental scenarios were considered:

- file download—20 MHz channel bandwidth (BW)
- file upload—20/40/80 MHz channel bandwidth performed by means of a free android application [41].

The E-field probe's sensing volume (pyramid tip) was positioned at 8 cm from the DUT, and the position of the DUT, probes, and router was kept constant during all measurements. Table 1 summarizes the main characteristics of the investigated experimental scenarios.

Table 1. Experimental scenarios considered.

No.	Communication Standard	Scenario	Channel's Central Frequency (MHz)	Channel's Bandwidth (ChBw) (MHz)
1	LTE-A	File upload	1750	20
2	LTE-A	Streaming	1750	20
3	LTE-A	Speed test	1750	20
4	IEEE 802.11ax	TCP Download	5220	20
5	IEEE 802.11ax	TCP Upload	5220	20
6	IEEE 802.11ax	TCP Upload	5230	40
7	IEEE 802.11ax	TCP Upload	5210	80

The measured power values were transformed into E-field strength values by applying (3) (extracted from the E-field probe calibration file provided by the manufacturer).

$$E\left(\frac{V}{m}\right) = 10\hat{}\left(\frac{P + 113.2 - 20 * lg(f)}{20}\right) \quad (3)$$

where P is the CP reading in dBm, and f represents the channel central frequency in MHz.

Afterwards, the total electric field strength can be computed as:

$$E_t = \sqrt{Ex^2 + Ey^2 + Ez^2} \quad (4)$$

where Ex, Ey, and Ez represent the time averaged electric field strengths (root mean square—RMS values) on the orthogonal directions.

If measurements are performed in far field condition, the knowledge of the E/H field strength solely is sufficient for calculating the power density (PD) by applying Equation (5) [3]:

$$PD = \frac{|E^2|}{\zeta_0} = \zeta_0 \left|H^2\right| \quad (5)$$

where ζ_0 is the characteristic impedance of free space.

The SDR measurement system was compared to solutions enabled using three SAs and a high bandwidth multichannel DO.

The SA model R&S FSL 13 was used for setting up the SA-enabled measurement system. Since simultaneous multichannel measurement is required, the system must use 3 SAs. Each E-field probe was connected to one SA which provided CP measurements. The 3 SAs were triggered by an external signal and the data were automatically retrieved via a custom-made Python application [42]. The experimental setup used for the SA measurement system is presented in Figure 5b.

The third measurement system was based on a 4-channel DO model R&S RTO6024 and is presented in Figure 7a. Each of the 3 E-field probes was connected to a dedicated DO input channel. The oscilloscope has a bandwidth of 6 GHz and a maximum sample rate of 20 G samples/s with a vertical resolution of up to 16 bits. When multiple channels are enabled, the oscilloscope bandwidth reduces to 4 GHz. The DO enables multi-channel spectrum analysis by performing fast Fourier transform (FFT) on the measured time samples. CP measurement option is also available. Remote measurements with the DO were performed via a Python application that also allowed automatic data retrieval. The measured CP values were saved to a file and further processed. In Figure 7b, we present a screenshot of the oscilloscope during the simultaneous measurements of the CP on all three channels.

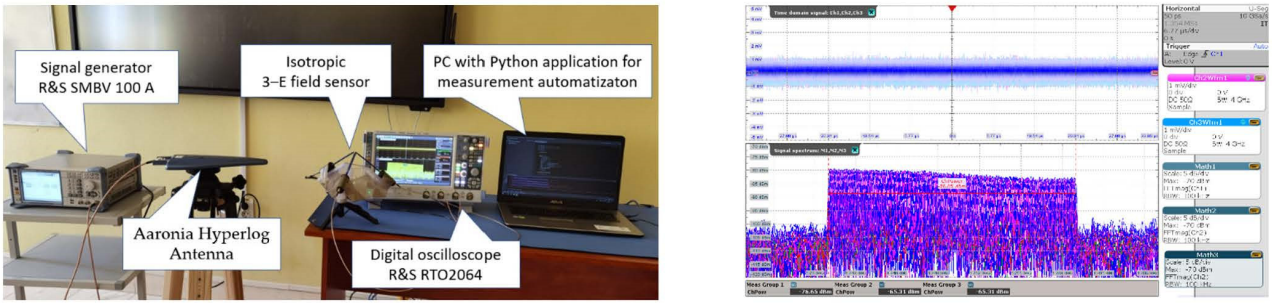

(**a**) (**b**)

Figure 7. (**a**) DO-enabled measurement system, (**b**) DO screen during a measurement activity.

3. Results

3.1. E-Field Sensor

Figure 8 presents the variation of all S parameters measured for the sensor.

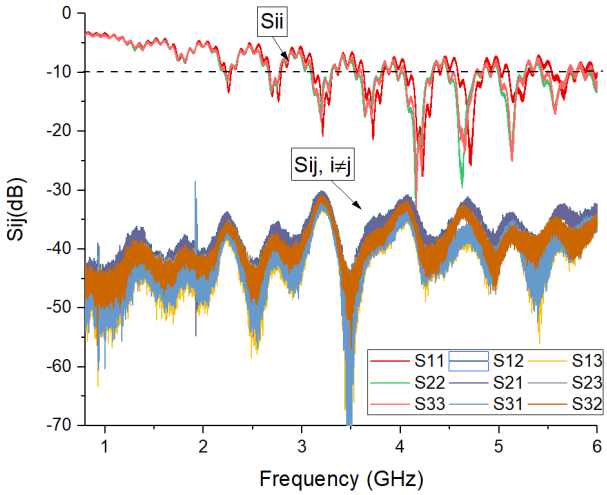

Figure 8. Variation with frequency of the reflection and transmission coefficients of the sensor elements when the mutual coupling is present.

The reflection coefficients (Sii) are higher at lower frequencies and the resonant frequencies are found mostly in the higher frequency range of the operating bandwidth. The S_{11} mean value is −9.06 dB, with a standard deviation of 3.93 dB and a minimum value of

−27.64 at the resonant frequency of 4222 MHz. In general, the figure shows a sufficiently good matching for the specific application.

Sij parameters are quite low (S_{12} mean value is −38.13 dB, with a standard deviation of 3.78 dB and a minimum value of −53.12 dB), indicating a small mutual coupling.

The estimation of the mutual coupling error based on Equation (1) is shown in Figure 9. The S_{21} data obtained from measurement were first transformed from dB to a natural value to be inputted to Equation (1), then converted back to dB and plotted in Figure 9.

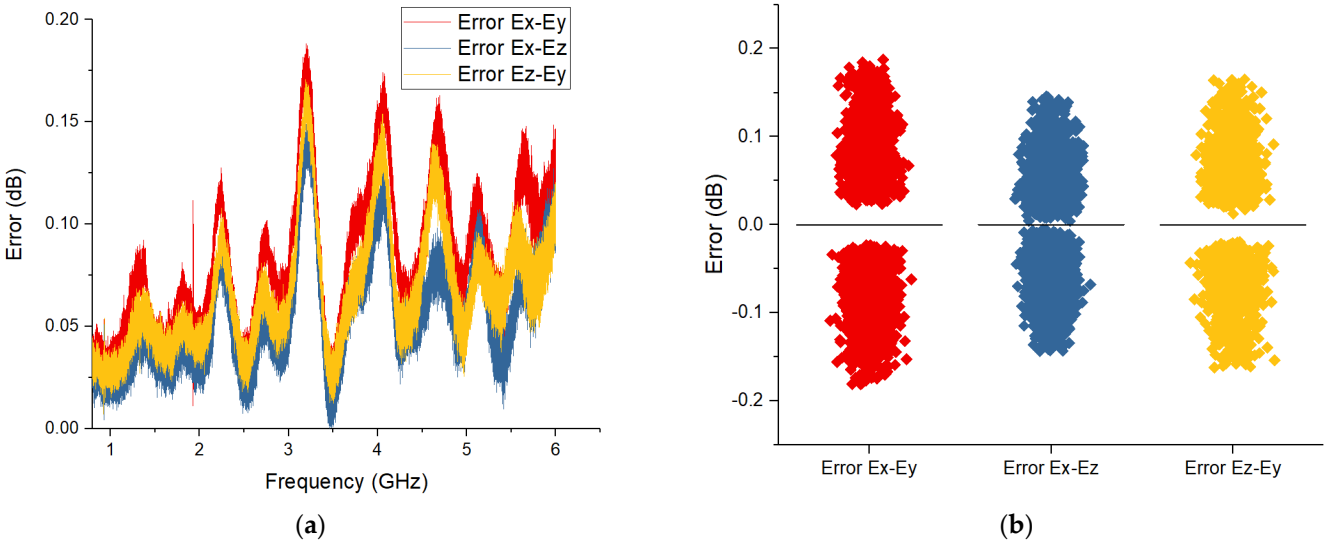

Figure 9. (**a**) Estimation of the error due to mutual coupling effect vs. frequency for all sensor elements. (**b**) Error variation boxplots.

The value is generally low, with a maximum error below 0.2 dB, confirming quite a small impact of the mutual coupling effects on the received signal.

Figure 10 presents the S_{11} measurement results for the patch antenna in the absence of an external perturbation, respectively, with the sensor placed in the vicinity of the antenna at distances of 1, 2, and 3 cm, respectively.

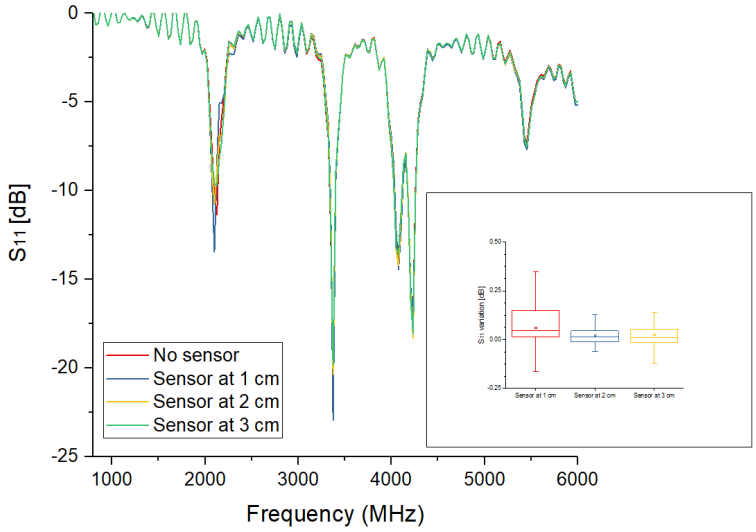

Figure 10. Patch antenna S_{11} parameter variation with frequency in different experimental scenarios.

Patch antenna S_{11} variation can be observed mainly around the antenna resonant frequencies. As the antenna has several resonant frequencies, the highest S_{11} variation (approximately 3 dB) occurs at the lowest frequency, and smallest distance from the antenna.

However, as the frequency increases, the S_{11} variation due to the sensor presence is reduced, and the mean S_{11} variation over the entire investigated frequency range was found to be 0.21 dB, 0.11 dB, and 0.08 dB for the three distances presented in the boxplots of Figure 10.

The field perturbation is expected to be proportional to the sensor dimensions, especially if metallic structures are used. One must keep in mind that the proposed sensor was manufactured using commercially available E-field probes, but in future developments, we will not exclude custom probe manufacturing which will enable miniature design and S_{11} parameters optimization.

3.2. Comparative Performances of the Measurement Instruments

An important characteristic of the measurement chain is the noise level present at the receiver. This becomes important for applications that require an adequate signal-to-noise ratio (SNR) when the signal to be measured has a low amplitude. For the three instruments, the noise power was chosen as the indicator of the sensitivity of the instrument.

The instrument noise power is composed of the thermal noise calculated according to Equation (6) and the noise figure of the instrument. The noise figure is the amount of noise power added by the electronic circuitry in the receiver to the thermal noise power from the input of the receiver. The thermal noise can be calculated based on Equation (6).

$$P_{termal\ noise}[dBm] = -173.8\ dBm + 10log_{10}(BW) \quad (6)$$

where BW is the channel bandwidth in Hz. To investigate the noise power and not to pick up RF signals from the environment, a 50 Ω termination was connected to the instrument RF channel input.

In Figure 11a we have represented the average value of the noise power for the three measurement instruments together with the calculated thermal noise limit. The noise power was measured using the CP over several bandwidths between 1.6 and 100 MHz. The channel central frequency was set to 2 GHz, while at the SA and DO, the resolution bandwidth (RBW) was set to 100 kHz. As theoretically expected, and described by Equation (6), the noise power increases with the channel bandwidth, resulting in the highest CP levels. The noise figures of all instruments follow the thermal noise variation with the bandwidth. One must note that the CP power measured by the SDR instrument is not calibrated and outputted in dB without an absolute reference power. Calibration can be easily performed by changing a multiplication constant value in the GNU Radio flowgraph presented in Figure 6. A detailed analysis of an in-house coarse calibration procedure can be found in [28].

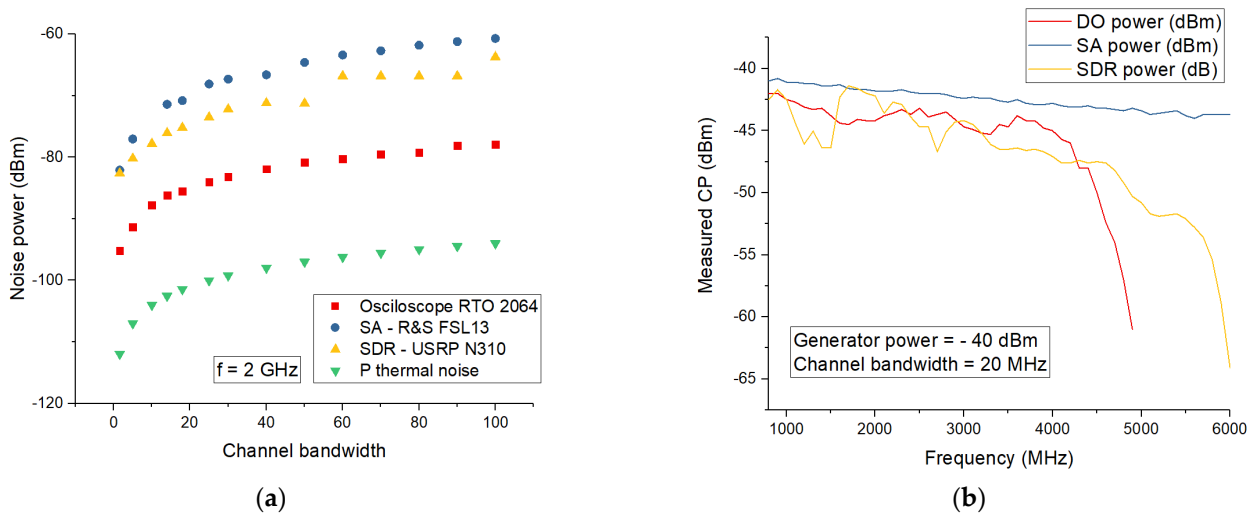

Figure 11. (**a**) Channel power of noise floor level at different channel bandwidths with different instruments. (**b**) Channel power of LTE signal—variation with frequency as measured by the three instruments.

The lowest noise figure for the channel power measurements can be observed for the DO. This is because of the low oscilloscope resolution used (eight bits—maximum available) combined with the minimum vertical scale setting of the oscilloscope (1 mV/div). The increase in the vertical scale will automatically increase the CP level. Usually, the measured signals do not exceed 20 mV (maximum amplitude) which makes it possible to use a vertical scale of 4 mV/div (to optimally use the available vertical resolution) that increases the measured CP by 2–3 dB. Another possibility to increase the sensitivity of the DO is to use a lower filter bandwidth (below 1 GHz). The filter reduces the noise, thereby increasing the SNR. However, this option is not as feasible for high-frequency signals as those used in up-to-date appliances that require the use of the maximum available channel bandwidth (4 GHz).

In Figure 11b we have represented the measured CP by the three measurement instruments over the frequency range 800–6000 GHz. For this experiment, a 20 MHz uplink LTE signal having a power of −40 dBm was configured at the signal generator. The signal generator was directly connected by cable to the measurement instrument channel. We can observe that the SA measured CP presents the flattest and most accurate reading. For the SA, the deviation from the true value of −40 dBm is due to cable loss, which increases with the frequency. The DO presents a higher deviation from the reference power level, but it is still capable to correctly indicate the CP. The deviation of the DO-measured CP from the SA-measured CP does not exceed 3 dB for frequencies below 4 GHz. Above 4 GHz, one can observe the rapid degradation of the DO performances, because of the maximum bandwidth limitation of 4 GHz that acts as a low pass filter for the measured signal. The SDR-indicated CP was calibrated for the 1.75 GHz frequency by setting a proper value of the multiplication constant in the Gnu Radio flowgraph. At the calibrated frequency, one can observe very good agreement between the SDR-measured CP and the SA-indicated CP. However, the SDR calibration does not remain valid for the entire frequency range and a new calibration must be performed if the operating frequency is changed [28].

In Figure 12, we have represented the results of the SDR calibration in two frequency bands: 3.3–3.7 GHz and 5–5.9 GHz. The two frequency bands were chosen as they are used for the 5G NR FR1 communication and the 5 GHz Wi-Fi standards. The top graphs present the comparative channel power values measured by the SA and the SDR across the investigated frequency bands, while in the bottom graphs, there are boxplots of CP variation. We can observe that we obtained very good agreement between the SDR and SA values. As expected, the values are more spread for the second frequency band (Figure 12 right) as in this case, the calibration bandwidth was of 1 GHz. Even so, we observe that most of the values in the entire frequency band (first to third quartile) exhibit a small variation from the median (<1 dB). The lower the calibration bandwidth the better the calibration result. To this extent we consider that this type of SDR demonstrates a satisfactory frequency response as the currently used RF channels are as highs as 100 MHz (5G NR FR1) or 160 MHz (IEEE 802.11ax standard).

Based on the measurement instrument performances, we have conducted a comparative analysis of the proposed multichannel measurement system. Table 2 presents the comparative analysis of the measurement system based on their hardware and software requirements, flexibility, cost, and investigated performance. The criteria were selected based on their suitability for in situ measurements of EMF emitted in the vicinity of present-day RF communication devices.

One should keep in mind that SDR instruments cannot be considered as reliable and accurate as traditional measurement instrumentation. As can be observed in Figure 11, SA measurement systems present the highest performances in terms of the displayed average noise level (DANL) and accuracy. However, to perform synchronous multichannel measurements, we need a significant number of measurement instruments (three in the presented scenario if SA are to be used). This results in excessive costs, reduced mobility, and scarce flexibility. These issues make such a measurement system unsuitable for in situ measurements, near an emitting device in various operating environments.

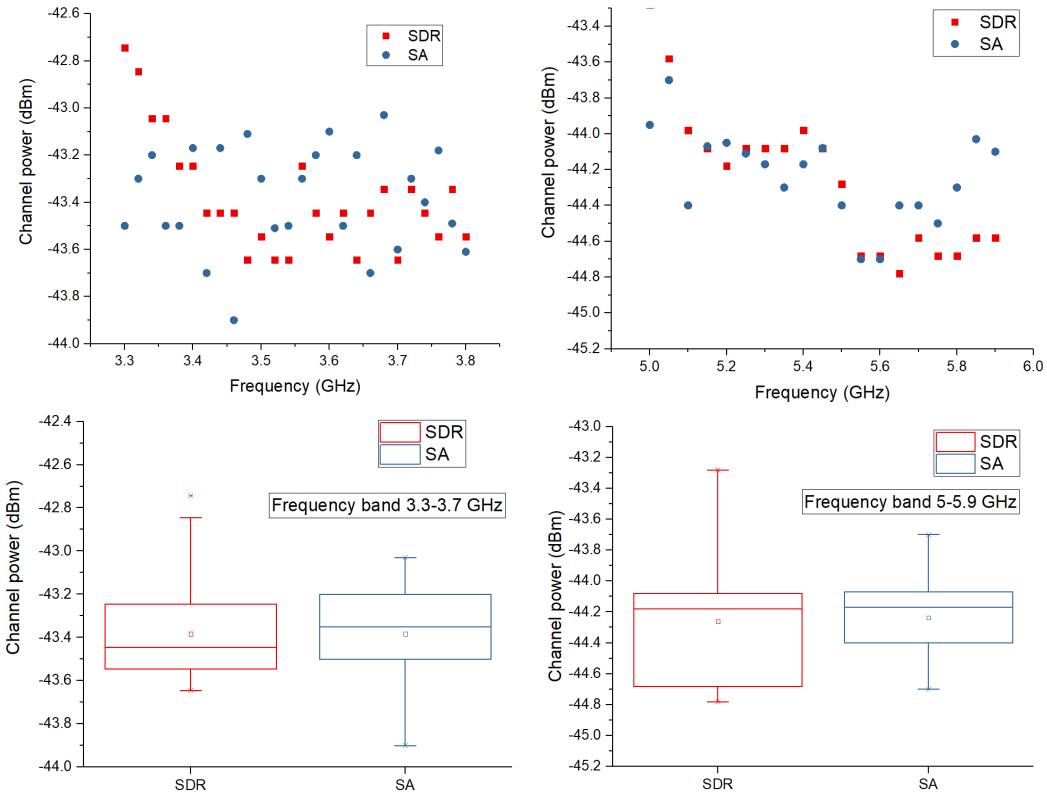

Figure 12. SDR calibration results in 3.3–3.7 GHz frequency band (**left**) and 5–5.9 GHz frequency band (**right**).

Table 2. Comparative analysis of the measurement systems.

Criteria		SDR-Enabled Measurement System	SA-Enabled Measurement System	DO-Enabled Measurement System
Hardware requirements		• E-field sensor • 1 × USRPs • Computer with fiber optic network card for 10 GB link with USRP	• E-field sensor • 3 × SAs • 3 × Computers for remote control measurements • External signal source for triggering	• E-field sensor • 1 × DOs • Computer for remote control measurements • External signal source for triggering
Software requirements		GNU Radio (open source) application	Python application for remote control process	Python application for remote control process
Flexibility		Medium	Reduced	Medium
Performance	DANL	Good	Good	Best
	Accuracy	Good, can be improved if previously calibrated	High	Good but limited to sub 4 GHz frequency range
Cost (Euro)		17,000	63,500	33,500

The recent technological development of DOs made it possible for these instruments to be used for frequency domain measurements also. We have studied the suitability of using a high performance DO for synchronized multichannel RF measurements. The current capabilities of the DO enables CP measurements for frequencies lower than the maximum available oscilloscope bandwidth. The limitations imposed by the DO-enabled measurement system relate to the instrument response time, the maximum available sample

rate, and the bandwidth. At the current technological development these limitations are often insufficient, especially for higher frequency applications.

Therefore, the SDR receiver has several advantages in terms of hardware and software requirements, cost, and flexibility. In addition, we obtained similar performances of the SDR-enabled measurement system as compared to the traditional approaches considered. Even so, the use of the SDR implies other problems that need careful solving. These problems refer mainly to the calibration of the amplitude response, for which we have used a simplified but effective procedure. After calibration, the SDR measurement system becomes an agile solution for the targeted EMF measurement campaigns, as proved by the results presented in the following subsection.

3.3. LTE-A and IEEE 802.11ax Signals Measurements

In Figure 13 we have represented the temporal evolution of the field strengths for the LTE-A speed test and streaming scenarios presented in Table 1. For the reported results, the averaging was performed over 10,000 signal samples, corresponding to 0.5 ms at a signal sampling rate of 20 MHz. Good synchronization was obtained between the values measured by the three enabled SDR channels marked by red, blue, and yellow traces, mostly visible at the beginning of a transmission session for both the speed test and streaming. The absolute field strengths measured by the E-field probes differ on the three considered channels, with probes measuring on the Oy and Ox direction being positioned closer to the DUT as compared to the probe measuring on the Oz direction.

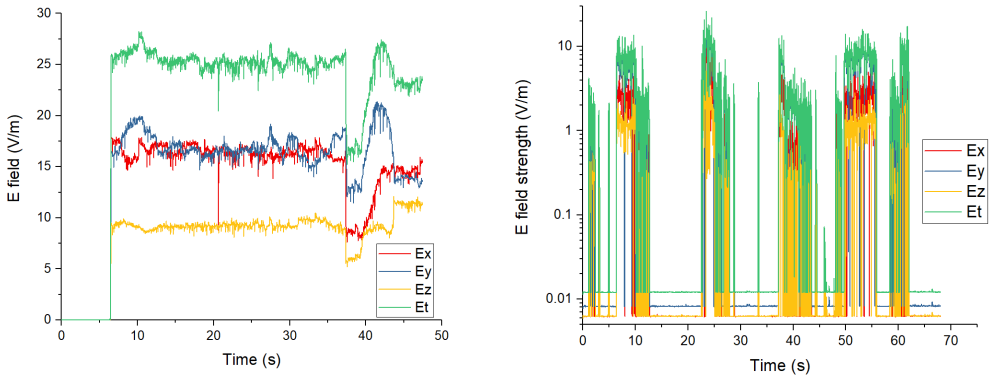

(**a**) (**b**)

Figure 13. Time evolution of Ex, Ey, Ez, and Etotal for LTE-A speed test (**a**) and streaming (**b**).

In Figure 14, we have represented the temporal evolution of the field strengths for the 802.11ax file download (a) and file upload—20 MHz ChBw (b) cases. We observe that the measured field values are below 1 V/m. For this communication standard, the measured field strengths are higher on the Ox axis followed by the Oz and Oy axis. As compared to the LTE-A scenario, this must be analyzed by taking into consideration the different antennas used by the DUT. The E-field values obtained for file upload are higher than for file download because during file upload, the DUT device is the emitting device, while for file download, it only sends acknowledgement frames and the Wi-Fi router is the emitting device.

In Figure 15, we have represented the temporal evolution of the field strengths for the LTE-A (a) and IEEE 802.11ax (b) experimental scenarios. For the LTE-A measured data, the speed test forces the LTE network resources in both the uplink and downlink direction and this resulted in the highest E-field strength values (29.8 V/m). The field values measured for streaming were the lowest even though streaming is a bandwidth-consuming application. Moreover, streaming resulted in the highest E-field variability as this type of service has low requirements in terms of network latency.

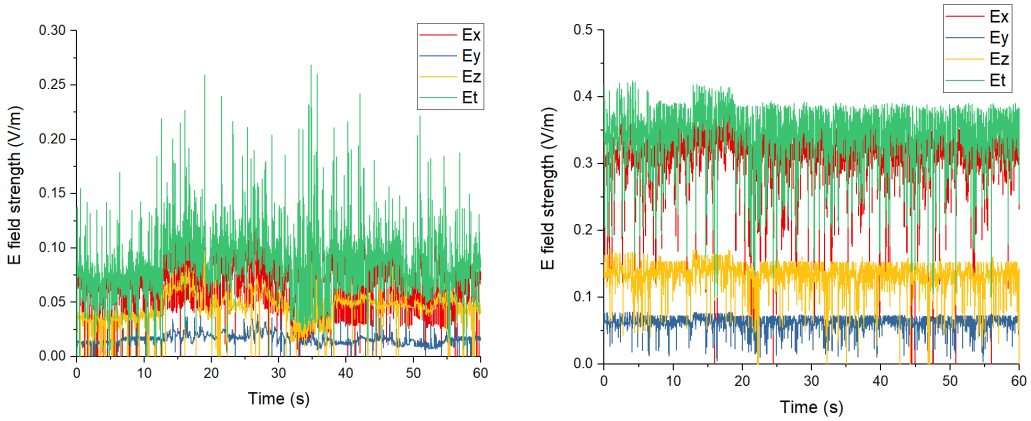

Figure 14. Time evolution of Ex, Ey, Ez, and Etotal for IEEE 802.11ax file download (**a**) and file upload 20 MHz (**b**).

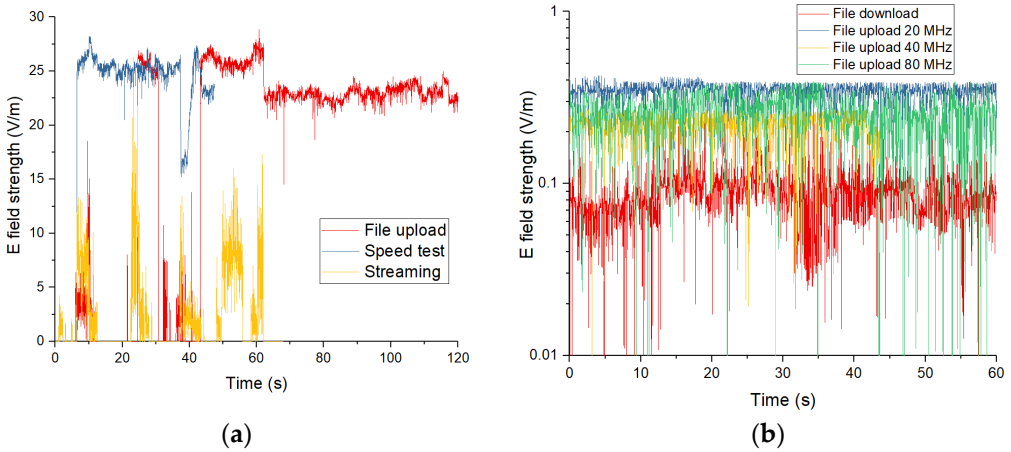

Figure 15. Time evolution of Efor LTE-A (**a**) and 802.11ax (**b**) experimental scenarios.

For the IEEE 802.11ax network, we have investigated the enabled SDR measurement system capabilities in continuous time retrieval of CP data for larger frequency bandwidths (40/80 MHz). As can be observed from Figure 15b the increase in channel bandwidth is not associated with a substantial modification of the measured field level as a result of the antenna parameter variation with the operating bandwidth.

4. Conclusions

The inherent temporal and spatial variability of the forthcoming generation of communication networks will require extensive in situ EMF measurements. To this extent, in this article, we have proposed a frequency-selective, true real-time, in situ EMF measurement system that can be used in the proximity of modern communication devices. The novelty of the approach is based on the capability of the designed system to synchronously measure both the E- and/or H-field components by using an efficient and agile solution destined specifically to highly dynamic stochastic signals. The system is composed of a sensor built from commercial off-the-shelf E-field probes and a multichannel SDR receiver. The simultaneous retrieval of the field components advances the current frequency-selective isotropic capabilities which, until now, were based on electronic switching (delay present) between the sensor elements. In this way, true real-time and spatial isotropic signal captures are possible, on the sub-microsecond time-variability scale. The proposed sensor geometry enables E-field strength retrieval on three orthogonal directions, in a small volume delimited by the sensor tips. The extension of the probe to the A/H field measurement is also briefly

discussed. A simplified analysis of the mutual coupling effect is carried out, showing the low impact of the mutual coupling on the signal level at the output of the probe.

The probe was connected to a multichannel SDR receiver. The proposed solution was compared in terms of performances, costs, and requirements to a standard solution enabled by SA and a DO. The three instruments' performances were evaluated comparatively based on their sensitivity (noise floor), accuracy, hardware and software requirements, flexibility, and cost. As a result, we demonstrate the similar performances of the proposed measurement system as compared to the traditional approach highlighting its advantages in terms of cost and flexibility.

Finally, the SDR-enabled measurement system was used for the in situ measurement of signals emitted by a mobile device in the LTE-A and IEEE 802.11ax communication standards. By using different experimental configurations, the proposed system demonstrates its capabilities in retrieving synchronous recordings of three RF channels up to an 80 MHz bandwidth. By conducting this research, we have demonstrated that the SDR technology offers a cost-efficient, agile solution for simultaneous multichannel EMF measurements that can be used for signals emitted in modern communication standards. The versatility of an SDR based solution was once more demonstrated in the case of a real-time, multichannel system designed for in situ EMF measurement campaigns.

Author Contributions: Conceptualization, A.S., M.D.M. and S.M.; Methodology, A.S., E.Ș. and M.Ș.; Software, P.B. and E.Ș.; Validation, A.S., S.M. and P.B.; Formal analysis, M.D.M.; Investigation, A.S., M.Ș. and E.Ș.; Writing—original draft preparation, A.S.; Writing—review and editing, A.S., S.M. and M.D.M.; Visualization, P.B. and M.D.M.; Supervision, S.M. and P.B.; Project administration, A.S.; Funding acquisition, A.S., S.M. and P.B. All authors have read and agreed to the published version of the manuscript.

Funding: This work was supported by a grant of the Romanian Ministry of Education and Research, CNCS—UEFISCDI, project number PN-III-P1-1.1-PD-2019-0500, within PNCDI III.

Conflicts of Interest: The authors declare no conflict of interest.

References

1. Mazar (Madjar), H. RF Human Hazards: Implementing 5G for Good: Does EMF Matter? In Proceedings of the ITU Regional Forum for Europe: 5G Strategies, Policies and Implementation, Warsaw, Poland, 22–23 October 2020.
2. Aerts, S.; Verloock, L.; Bossche, M.V.D.; Colombi, D.; Martens, L.; Tornevik, C.; Joseph, W. In-situ Measurement Methodology for the Assessment of 5G NR Massive MIMO Base Station Exposure at Sub-6 GHz Frequencies. *IEEE Access* **2019**, *7*, 184658–184667. [CrossRef]
3. Migliore, M.D.; Franci, D.; Pavoncello, S.; Grillo, E.; Aureli, T.; Adda, S.; Suman, R.; D'Elia, S.; Schettino, F. A New Paradigm in 5G Maximum Power Extrapolation for Human Exposure Assessment: Forcing gNB Traffic Toward the Measurement Equipment. *IEEE Access* **2021**, *9*, 101946–101958. [CrossRef]
4. ICNIRP. Guidelines for limiting exposure to time-varying electric, magnetic, and electromagnetic fields (up to 300 GHz). *Health Phys.* **2020**, *118*, 483–524. [CrossRef] [PubMed]
5. *C95.1-2019*; IEEE Standard for Safety Levels with Respect to Human Exposure to Electric, Magnetic, and Electromagnetic Fields, 0 Hz to 300 GHz. IEEE: New York, NY, USA, 2019. [CrossRef]
6. Alon, L.; Gabriel, S.; Cho, G.Y.; Brown, R.; Deniz, C.M. Prospects for Millimeter-Wave Compliance Measurement Technologies [Measurements Corner]. *IEEE Antennas Propag. Mag.* **2017**, *59*, 115–125. [CrossRef]
7. Schmid, T.; Egger, O.; Kuster, N. Automated E-field scanning system for dosimetric assessments. *IEEE Trans. Microw. Theory Technol.* **1996**, *44*, 105–113. [CrossRef]
8. Le, D.T.; Hamada, L.; Watanabe, S.; Onishi, T. An estimation method for vector probes used in determination SAR of multiple-antenna transmission systems. In Proceedings of the 2014 International Symposium on Electromagnetic Compatibility, (EMC'14/Tokyo), Tokyo, Japan, 4–8 August 2014; pp. 629–632.
9. Okano, Y.; Shimoji, H. Comparison measurement for specific absorption rate with physically different procedure. *IEEE Trans. Instrum. Meas.* **2012**, *61*, 439–446. [CrossRef]
10. Gladman, A.S.; Davidson, S.R.H.; Easty, A.C.; Joy, M.L.; Sherar, M.D. Infrared thermographic SAR measurements of interstitial hyperthermia applicators: Errors due to thermal conduction and convection. *Int. J. Hyperth.* **2004**, *20*, 539–555. [CrossRef]
11. Alon, L.; Cho, G.Y.; Yang, X.; Sodickson, D.K.; Deniz, C.M. A method for safety testing of radiofrequency/microwave-emitting devices using MRI. *Magn. Reson. Med.* **2015**, *74*, 1397–1405. [CrossRef]

12. Miclaus, S.; Bechet, P. Estimated and measured values of the radiofrequency radiation power density around cellular base stations. *Environ. Phys.* **2007**, *52*, 429–440.
13. Hodzic, V.; Gammon, R.W.; Balzano, Q.; Davis, C.C. *Rapid Optical SAR Measurements*; University of Maryland: College Park, MD, USA, 2016; Available online: https://www.ece.umd.edu/rrd/98-sarposterrrd09.pdf (accessed on 5 July 2022).
14. Foster, K.R.; Ziskin, M.C.; Balzano, Q. Three Quarters of a Century of Research on RF Exposure Assessment and Dosimetry—What Have We Learned? *Int. J. Environ. Res. Public Health* **2022**, *19*, 2067. [CrossRef]
15. Joseph, W.; Frei, P.; Roösli, M.; Thuróczy, G.; Gajsek, P.; Trcek, T.; Bolte, J.; Vermeeren, G.; Mohler, E.; Juhász, P.; et al. Comparison of personal radio frequency electromagnetic field exposure in different urban areas across Europe. *Environ. Res.* **2010**, *110*, 658–663. [CrossRef] [PubMed]
16. Vallauri, R.; Bertin, G.; Piovano, B.; Gianola, P. Electromagnetic field zones around an antenna for human exposure assessment: Evaluation of the human exposure to EMFs. *IEEE Antennas Propag. Mag.* **2015**, *57*, 53–63. [CrossRef]
17. Velghe, M.; Aerts, S.; Martens, L.; Joseph, W.; Thielens, A. Protocol for personal RF-EMF exposure measurement studies in 5th generation telecommunication networks. *Environ. Health* **2021**, *20*, 36. [CrossRef] [PubMed]
18. Lundgren, J.; Helander, J.; Gustafsson, M.; Sjoberg, D.; Xu, B.; Colombi, D. A Near-Field Measurement and Calibration Technique: Radio-Frequency Electromagnetic Field Exposure Assessment of Millimeter-Wave 5G Devices. *IEEE Antennas Propag. Mag.* **2021**, *63*, 77–88. [CrossRef]
19. Pfeifer, S.; Fallahi, A.; Xi, J.; Neufeld, E.; Kuster, N. Forward Transformation from Reactive Near-Field to Near and Far-Field at Millimeter-Wave Frequencies. *Appl. Sci.* **2020**, *10*, 4780. [CrossRef]
20. Available online: https://www.anritsu.com/en-us/components-accessories/products/2000-1791-r (accessed on 9 April 2022).
21. Available online: https://scdn.rohde-schwarz.com/ur/pws/dl_downloads/dl_common_library/dl_brochures_and_datasheets/pdf_1/TS-EMF_dat-sw_en_3608-9918-22_v0200.pdf (accessed on 6 July 2022).
22. Available online: https://www.wavecontrol.com/rfsafety/images/data-sheets/en/WaveMon_RF-60_Datasheet_EN.pdf (accessed on 9 April 2022).
23. Lipovac, A.; Lipovac, V.; Modlic, B. PHY, MAC, and RLC Layer Based Estimation of Optimal Cyclic Prefix Length. *Sensors* **2021**, *21*, 4796. [CrossRef]
24. Amado, J.; Fano, G. Antenna coupling model in receiving mode. In Proceedings of the 2016 IEEE Global Electromagnetic Compatibility Conference (GEMCCON), Mar del Plata, Argentina, 7–9 November 2016; pp. 1–5. [CrossRef]
25. Moraitis, N.; Popescu, I.; Nikita, K.S. Frequency Selective EMF Measurements and Exposure Assessment in Indoor Office Environments. In Proceedings of the 2020 14th European Conference on Antennas and Propagation (EuCAP), Copenhagen, Denmark, 15–20 March 2020; pp. 1–5. [CrossRef]
26. Chiaramello, E.; Bonato, M.; Fiocchi, S.; Tognola, G.; Parazzini, M.; Ravazzani, P.; Wiart, J. Radio frequency electromagnetic fields exposure assessment in indoor environments: A review. *Int. J. Environ. Res. Public Health* **2019**, *16*, 955. [CrossRef]
27. Jomaa, K. Electromagnetic Near-Field Characterization & Occupational Exposure to RF Waves in Industrial Environment. Ph.D. Thesis, Université Grenoble Alpes, Saint-Martin-d'Hères, France, 2018.
28. Sârbu, A.; Bechet, P.; Miclăuș, S.; Helbet, R.; Șorecău, E. Isotropic near field measurement system for new generation communication signals: Preliminary design and USRP calibration. In Proceedings of the 2021 International Conference on Applied and Theoretical Electricity (ICATE), Craiova, Romania, 27–29 May 2021; pp. 1–5. [CrossRef]
29. Helbet, R.; Bechet, P.; Monda, V.; Miclaus, S.; Bouleanu, I. Low-Cost Sensor Based on SDR Platforms for TETRA Signals Monitoring. *Sensors* **2021**, *21*, 3160. [CrossRef]
30. Available online: https://aaronia.com/antennas/rf-and-near-field-probes/ (accessed on 3 April 2022).
31. Balanis, C.A. *Antenna Theory, Analysis and Design*, 1st ed.; John Wiley & Sons: New York, NY, USA, 1982.
32. Collin, R.E. *Foundations for Microwave Engineering*, 2nd ed.; Wiley-IEEE Press: New York, NY, USA, 2000.
33. Perotoni, M.B.; Silva, L.A.; Silva, W.; Santos, K.M.G. Near-Field Measurement System Based on a Software Defined Radio. *Prog. Electromagn. Res. Lett.* **2022**, *102*, 87–94. [CrossRef]
34. Abbas, Y.M.O.; Asami, K. Design of Software-Defined Radio-Based Adaptable Packet Communication System for Small Satellites. *Aerospace* **2021**, *8*, 159. [CrossRef]
35. Armas Jiménez, S.; Sanchez-Garcia, J.; Castillo-Soria, F.R. Self Interference Cancellation on a Full Duplex DFTs-OFDM System using GNU Radio and USRP. *IEEE Lat. Am. Trans.* **2021**, *19*, 1781–1789. [CrossRef]
36. Avuthu, A.R.; Battula, R.B.; Gopalani, D. An efficient spectrum sensing over η-μ fading on sub 6 GHz bands: A real-time implementation on USRP RIO. *Wirel. Netw.* **2022**, *28*, 2567–2577. [CrossRef]
37. Cao, K.; Jiang, M.; Gao, S. Spectrum availability prediction based on RCS-GRU model. *Phys. Commun.* **2021**, *49*, 101479. [CrossRef]
38. Zhang, L.; Lin, C.; Yan, W.; Ling, Q.; Wang, Y. Real-Time OFDM Signal Modulation Classification Based on Deep Learning and Software-Defined Radio. *IEEE Commun. Lett.* **2021**, *25*, 2988–2992. [CrossRef]
39. Bechet, A.C.; Helbet, R.; Bouleanu, I.; Sarbu, A.; Miclaus, S.; Bechet, P. Low Cost Solution Based on Software Defined Radio for the RF Exposure Assessment: A Performance Analysis. In Proceedings of the 2019 11th International Symposium on Advanced Topics in Electrical Engineering (ATEE), Bucharest, Romania, 28–30 March 2019. [CrossRef]
40. Available online: https://consumer.huawei.com/uk/community/details/App-Gallery-Speedtest-by-Ookla/topicId_38770/ (accessed on 5 July 2022).

41. PZolee's Blog. Available online: http://pzoleeblogen.wordpress.com/2013/11/26/wifi-speed-test-for-androidhow- (accessed on 5 July 2022).
42. Paljanos, A.; Miclăuș, S.; Bechet, P.; Munteanu, C. Assessment of mobile phone user exposure to UMTS and LTE signals: Comparative near-field radiated power levels for various data and voice application services. *J. Electromagn. Waves Appl.* **2016**, *30*, 1101–1115. [CrossRef]